

# Synthetic Aperture Sensing for Occlusion Removal with Drone Swarms

Rakesh John Amala Arokia Nathan<sup>1</sup>, Indrajit Kurmi<sup>1</sup> and Oliver Bimber<sup>1\*</sup>

<sup>1</sup>Computer Science Department, Johannes Kepler University Linz, 4040, Austria.

\*Corresponding author(s). E-mail(s): [oliver.bimber@jku.at](mailto:oliver.bimber@jku.at);

Contributing authors: [rakesh\\_john.amala\\_arokia\\_nathan@jku.at](mailto:rakesh_john.amala_arokia_nathan@jku.at); [indrajit.kurmi@jku.at](mailto:indrajit.kurmi@jku.at);

## Abstract

We demonstrate how efficient autonomous drone swarms can be in detecting and tracking occluded targets in densely forested areas, such as lost people during search and rescue missions. Exploration and optimization of local viewing conditions, such as occlusion density and target view obliqueness, provide much faster and much more reliable results than previous, blind sampling strategies that are based on pre-defined waypoints. An adapted real-time particle swarm optimization and a new objective function are presented that are able to deal with dynamic and highly random through-foliage conditions. Synthetic aperture sensing is our fundamental sampling principle, and drone swarms are employed to approximate the optical signals of extremely wide and adaptable airborne lenses.

**Keywords:** occlusion removal, through-foliage, particle-swarm optimization, sampling, synthetic aperture sensing

Drone swarms often explore a collaborative behaviour to perform as an intelligent group of individuals and achieve objectives that would be impossible or impractical to achieve individually [1–5]. Single drones within the swarm can perceive their local environment and then act accordingly with or without direct awareness of the swarm’s overall objective. They have been used for surveillance and environment mapping [6–13], airbase communication networking [14–18], infrastructure inspection and construction [19–21], or load transport and delivery [22], and are particularly useful in areas that are not easily accessible by humans, such as forests and disaster sites [23–25].

Drone swarms utilize either a centralized control system [7, 8, 11, 18] (where either an omniscient drone or an external computer performs communication and pre-plans actions) or a decentralized control system [6, 10, 13, 15, 21, 25] (drones

communicate with each other and make decisions locally). Hand-crafted [1, 29–34] or automatically designed algorithms (e.g., heuristics-based, evolutionary-based, learning-based [1, 2, 35–55]) have been applied to implement various swarm behaviours (e.g., flocking, formation flight and distributed sensing) for achieving a desired objective (e.g., path planning, task assignment, flight control, formation reconfiguration and collision avoidance).

Meta-heuristic algorithms (e.g., genetic algorithms, differential-equation-based algorithms, ant-colony and particle swarm optimization) exploit non-Markovian properties of a problem (i.e., each individual drone has only a partial observation of the swarm). Their inherent ability to deal with credit assignment has led to these approaches being

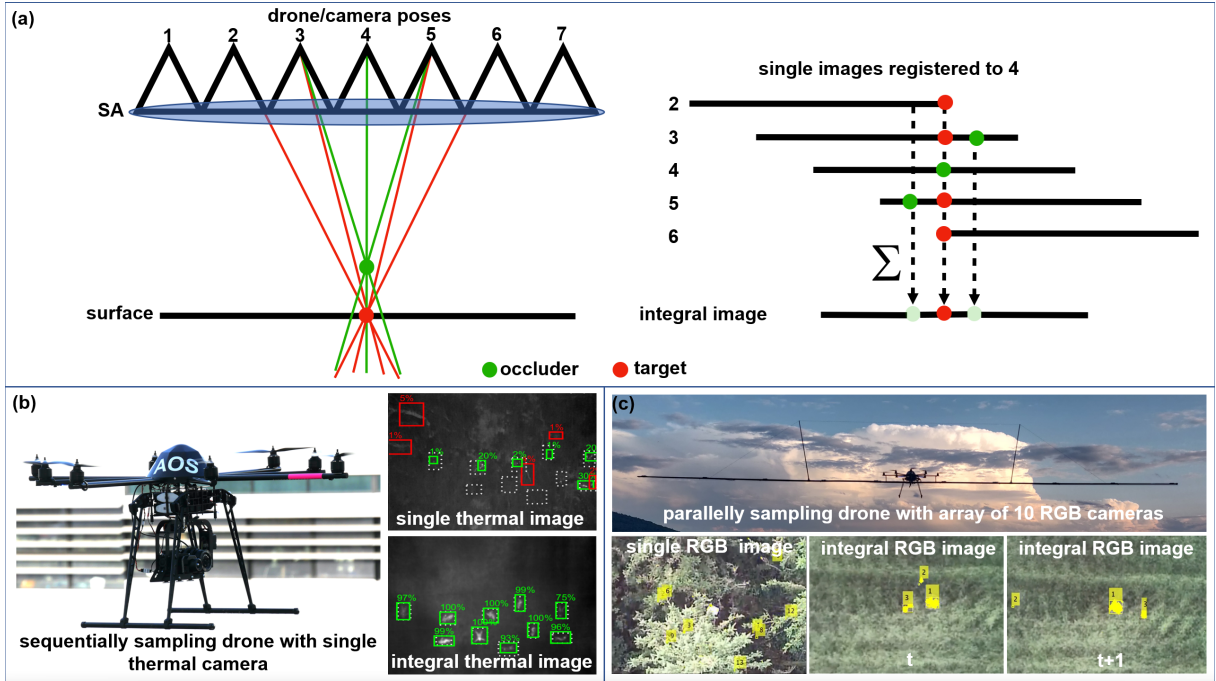


**Fig. 1** AOS sampling principle (a): After image registration and integration, misaligned occluders above the focused ground surface are suppressed, while aligned targets on the ground surface are emphasized. A single camera drone prototype that sequentially samples the SA to detect static targets (persons lying on the ground) in a dense forest [26, 27] (b). A drone prototype with a parallelly sampling camera array that spans a 10 m wide 1D SA supports detection and tracking of moving targets (walking persons) in a dense forest [28] (c). Classification (b) as well as anomaly detection and tracking (c) through foliage becomes possible in integral images while it remains unfeasible in single images (with many false positives and true negatives).

more widely adopted than classical and learning-based algorithms (e.g., deep-learning neural network, reinforcement-learning) in the swarm literature. Particle swarm optimization (PSO) in particular is computationally efficient, robust, and can be incorporated into hierarchical planning structures.

Synthetic aperture (SA) sensing is a signal processing technique which takes measurements of limited size sensors and improves them by computationally combining their samples to mimic sensor apertures of physically impossible width. In recent decades, it has been applied in various fields, such as radar [56–58], radio telescopes [59, 60], interferometric microscopy [61], sonar [62, 63], ultrasound [64, 65], LiDAR [66, 67], and imaging [68–75].

With Airborne Optical Sectioning (AOS) [26–28, 76–84], we have introduced an optical synthetic aperture imaging technique for removing partial occlusion caused by vegetation (cf. Fig. 1a). Drones equipped with conventional cameras are used to sample images above forest. These images have a wide depth of field, due to the cameras’ narrow

apertures (i.e., small lenses, usually a few millimeters). They are registered and integrated to mimic shallow depth of field images as would have been captured by a very wide aperture camera (using a lens that covers the sampling area, several meters in diameter). Computationally focusing the resulting integral image on the forest ground by registering the single images appropriately with respect to the drones’ sampling positions emphasizes the targets’ signal while very quickly suppressing (due to the shallow depth of field) the signals of occluders above. The unique advantages of AOS, such as its real-time processing capability and wavelength independence, opens many new application possibilities in contexts where occlusion is problematic. These include, for instance, search and rescue, wildlife observation, wildfire detection, and surveillance. We have demonstrated that image processing techniques, such as classification [26] and anomaly detection [28], are significantly more efficient in the presence of occlusion when applied to integral images rather than to single images.



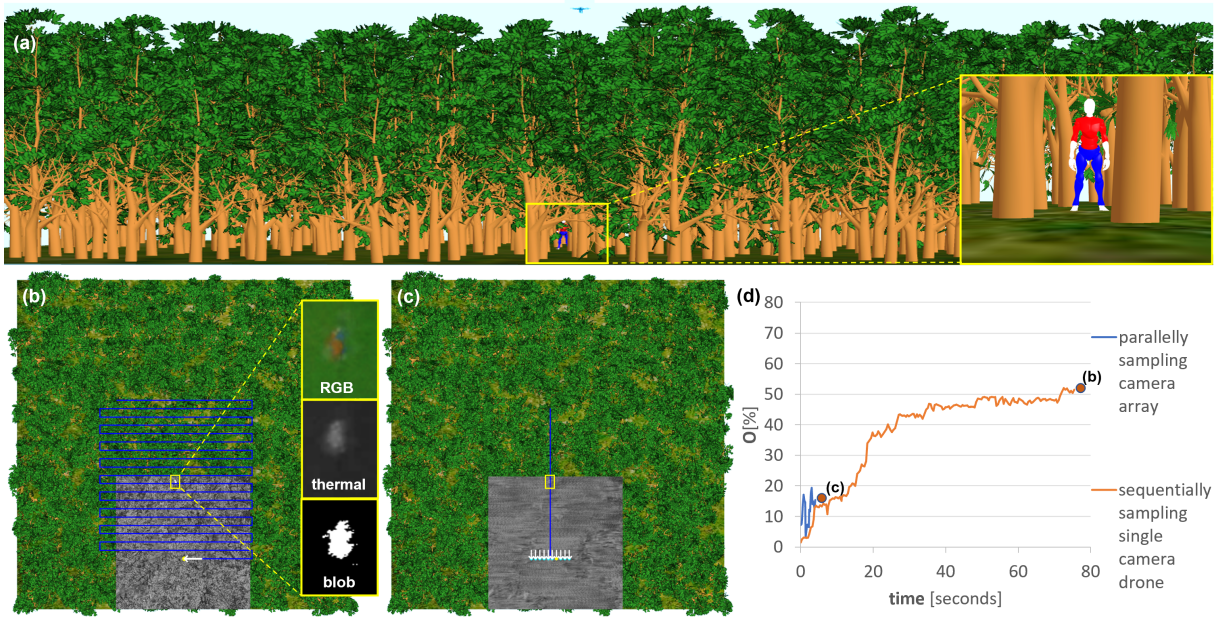


**Fig. 2** Our simulation environment was a 1 ha procedural forest with one hidden avatar (a). Blind brute-force sequential sampling (b), as in the case of a single camera drone that sequentially samples the SA (Fig. 1b) [26], led to a maximum target visibility (*MTV*) of 51% after a long period of 75 seconds (d). Blind parallel sampling (c), as with an airborne camera array (Fig. 1c) [28], was fast, but resulted in only 19% *MTV* after a short period of 3 seconds (d). Our objective function  $O$  models target visibility by the contour size of the largest connected pixel cluster (blob) computed from anomalies in color (RGB) and thermal channels, as explained in **Objective Function**. Note that the yellow boxes highlight the target, the white arrows show the movement of the drones between time steps  $t - 1$  and  $t$ , the blue lines represent the total sampling paths, and the grey area shows the integrated ground coverage at time  $t$ . Simulation parameters: drone's ground speed = 10 m/s, forest density = 300 trees/ha, single camera drone (b) sampling sequentially a  $36 \times 38$  m SA with a  $4 \times 2$  m resolution, array of 10 cameras (c) sampling at 1 m inter-camera distance with 2 m steps in the flight direction (as shown for the prototype in Fig. 1c). See Supplementary Video 2.

We have previously presented several sampling techniques for AOS. Early approaches used single, sequentially sampling drones that followed pre-defined waypoints [26, 76–83] or autonomously determined flight paths that were dynamically planned based on classification results [27] (cf. Fig. 1b). Sequential sampling does not support moving targets, as long sampling periods result in strong motion blur. Initially, parallel sampling strategies were investigated which used large 1D camera arrays with a fixed sampling pattern instead of single cameras (cf. Fig. 1c). They supported motion detection and tracking, but were cumbersome to handle, difficult to fly stably, and result in undersampled integrals. In all of these cases, varying forest properties, such as changing local occlusion densities, could not be considered for optimized sampling. Due to their high complexity, local viewing conditions could not be reconstructed in real time during scanning, and were impossible to model or learn because of

their high degree of randomness. However, knowing sparser forest patches through which targets could be observed with less occlusion and possibly even from more oblique viewing angles could make AOS sampling significantly more efficient than sampling blindly. The sampling pattern could then adapt adequately and dynamically to local viewing conditions.

In this article, we demonstrate that particle swarm optimization (PSO) is a suitable instrument for solving this problem. Here, we consider an autonomous swarm of drones that explores optimal local viewing conditions for AOS sampling. They approximate the optical signal of extremely wide and adaptable airborne lens apertures (see supplementary Video Abstract).

While PSO has a long history in modeling real-time swarm behaviour [44–55], the objective function for AOS is not constant (especially in the case of target motion), highly random (forest occlusion),

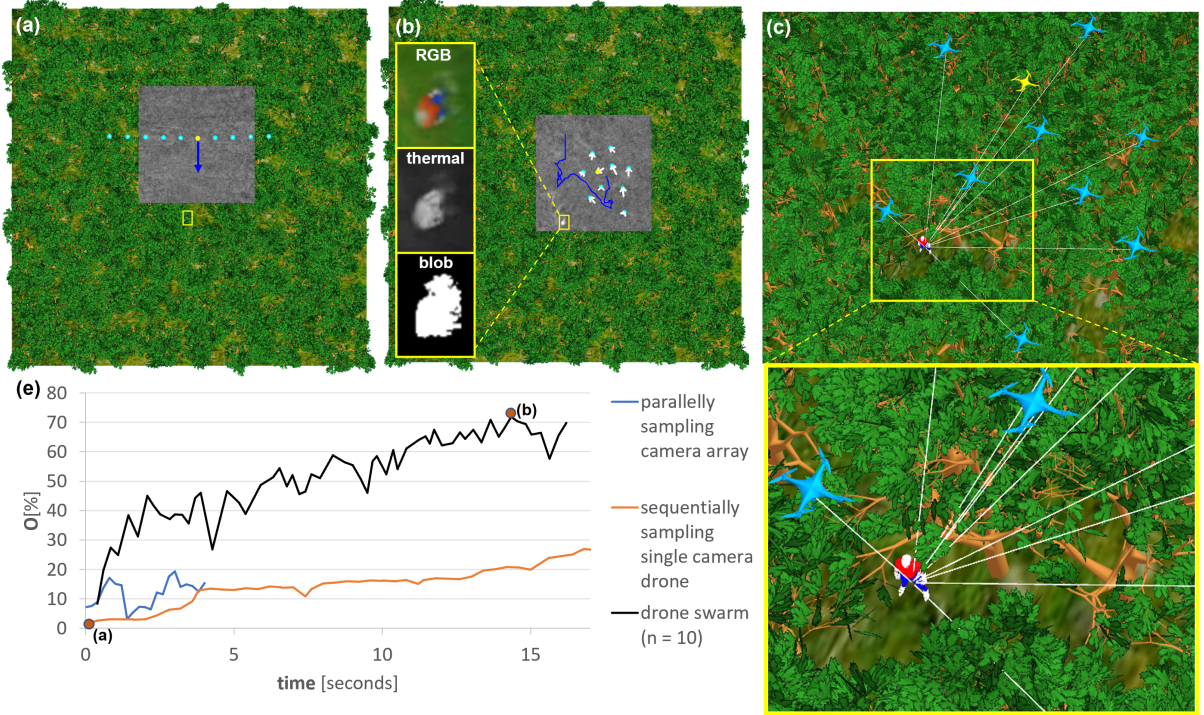


**Fig. 3** Swarm of 10 drones approaches target in default (linear) scanning pattern (a) and then converges (b) to maximize target visibility (e). Our objective function  $O$  models target visibility by the contour size of the largest connected pixel cluster (blob) computed from anomalies in color (RGB) and thermal channels (b). A maximum target visibility ( $MTV$ ) of 72% was reached after 14 seconds (e) by finding and converging above gaps in the vegetation, as shown in the close-ups (c,d). For comparison, the blind sampling results from Fig. 2 are also plotted for the same duration in (e). Note that the white rays indicate direct line of sight between drones and target, the yellow boxes highlight the target, the white arrows show the movement of the drones between time steps  $t - 1$  and  $t$ , the blue lines represent the total sampling paths of the swarm's center of gravity, the yellow dots/drones indicate the best sampling position at time  $t$ , and the grey area shows the integrated ground coverage at time  $t$ . Simulation parameters (see **Methods** for details): drones' ground speed = 10 m/s, forest density = 300 trees/ha,  $n = 10$ ,  $T = 16.3\%$ ,  $\Delta_h = 1$  m,  $h_1 = 35$  m,  $c_1 = 1$  m,  $c_2 = 2$  m,  $c_3 = 2$  m,  $s = c_4 = 4.2$  m,  $c_5 = 0.3$ . See Supplementary Video 3.

neither linear nor smooth, and certainly not differentiable. We present a PSO variant and a new objective function that can cope with these challenges and that considers additional sampling constraints, such as enforcing minimal sampling steps because smaller ones would not contribute to occlusion removal [77, 80]. Furthermore, we explain how PSO hyper-parameters are directly related to SA properties, such as the aperture diameter, and show that collision avoidance can be achieved by simple altitude offsets without significant reduction in sampling quality.

Experiments reveal that, in contrast to previous blind sampling strategies which are based on pre-defined waypoint flights (where sampling is either sequential or parallel), drone swarms adapt to optimal viewing conditions, such as low occlusion density and large target view obliqueness (which

increases the projected footprint of the target). Furthermore, they combine sequentially and parallelly recorded samples. Both increases visibility significantly while reducing sampling time. Lastly, moving targets can be detected and tracked even under difficult through-foliage conditions.

Our approach using autonomously exploring swarms of drones can lead to faster and much more reliable detection of strongly occluded targets, such as missing persons in search and rescue missions, animals during wildlife observation, hot-spots during wild-fire inspections, or security threats during patrols.

## Results

We applied a procedural forest model (cf. Fig. 2a) to simulate the AOS sampling process in four spectral bands (visible and far infrared, RGB+thermal),



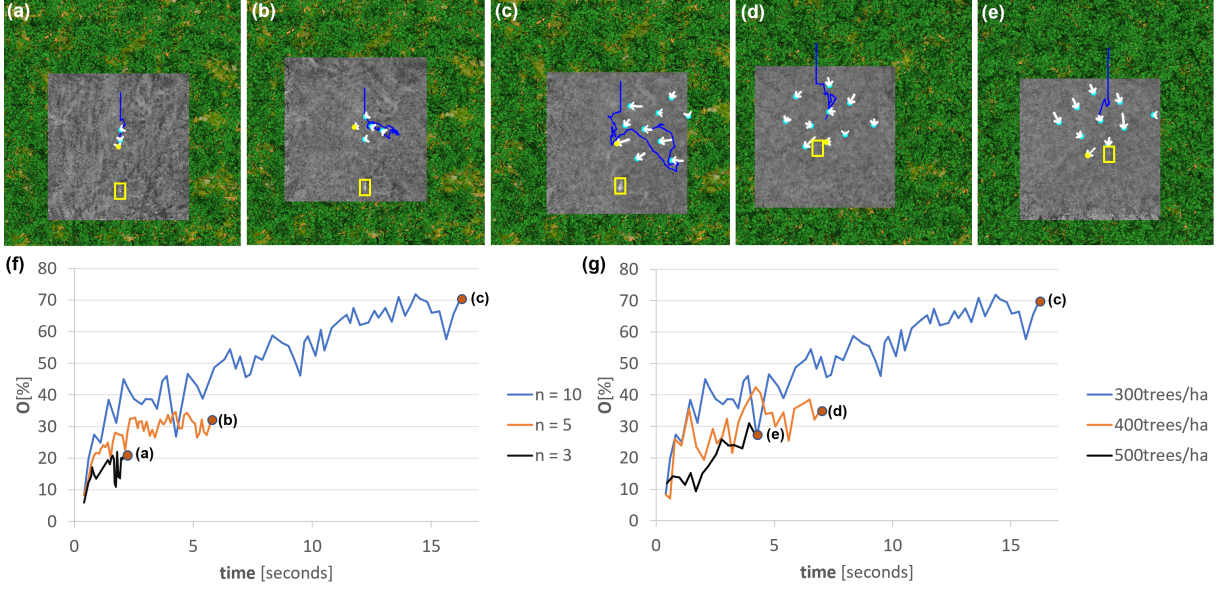


**Fig. 4** Increasing swarm size ( $n=3,5,10$  in a,b,c) led to better target visibility (f). Here, a wider synthetic aperture and a larger number of samples increased the target visibility and consequently the probability of its detection. Increasing forest density (300, 400, 500 trees/ha in c,d,e) decreased target visibility due to denser occlusion. Here, the swarm size was constant ( $n=10$ , as in Fig. 3). Note that the yellow boxes highlight the target, the white arrows show the movement of the drones between time steps  $t-1$  and  $t$ , the blue lines represent the total sampling paths of the swarm's center of gravity, the yellow dots indicate the best sampling position at time  $t$ , and the grey area shows the integrated ground coverage at time  $t$ . Note also that the plots end in case of no further visibility improvement. Simulation parameters (see **Methods** for details): drones' ground speed =  $10\text{ m/s}$ ,  $\Delta_h = 1\text{ m}$ , forest density = 300 trees/ha (a-c) / 400 trees/ha (d) / 500 trees/ha (e),  $n=3$  (a) / 5 (b) / 10 (c-e),  $T = 7.93\%$  (a) / 11.19% (b) / 16.3% (c) / 8.86% (d) / 8.39% (e),  $h_1 = 38\text{ m}$  (a) / 39 m (b) / 35 m (c-e),  $c_1 = 0.22\text{ m}$  (a) / 0.445 m (b) / 1 m (c) / 1 m (d) / 1 m (e),  $c_2 = 0.44\text{ m}$  (a) / 0.89 m (b) / 2 m (c) / 2 m (d) / 2 m (e),  $c_3 = 2\text{ m}$  (a-e),  $s = c_4 = 0.933\text{ m}$  (a) / 1.87 m (b) / 4.2 m (c) / 4.2 m (d) / 4.2 m (e),  $c_5 = 0.3$  (a-e). See Supplementary Video 4.

for different forest occlusion densities and sampling procedures (parallel, sequential, single drones, camera arrays, swarms), as well as for moving and static targets. Implementation details are summarized in **Implementation**, and a comparison between simulated and real integral images is provided in **S1** of the supplementary material. All experiments were evaluated with the objective function presented in **Objective Function**. It determines the target visibility, and we consider it in % (given that the highest visibility of an unoccluded target is known and 100%). Note that the maximum target visibility ( $MTV$ ) under occlusion over the entire sampling time provides the best hint of a potentially detected target. Our PSO approach with its collision avoidance strategy and hyper-parameters are explained in **Particle Swarm Optimization, Collision Avoidance**, and **Hyper-Parameters**. We conclude with a discussion of the results in **Discussion and Conclusion**.

The goal of the following experiments was automatic detection of a standing or walking person

in occluding forest. We compare different sampling options for this task: (1) a single sequentially sampling drone (as shown in Fig. 1a) following a predefined 2D search grid at constant altitude (40 m AGL), (2) an airborne array of 10 parallelly recording cameras (as shown in Fig. 1b) while following a predefined 1D search path at constant altitude (40 m AGL), and (3) swarms of 3, 5, and 10 drones following our PSO at various individual altitudes for collision avoidance (swarm average altitude is always 40 m AGL), as explained in **Collision Avoidance**. In all cases, starting conditions and flight speed ( $10\text{ m/s}$ ) were identical, and the images captured (sequentially and parallelly) were integrated in overlapping ground surface regions. We also investigated different forest densities: sparse (300 trees/ha), medium (400 trees/ha), and dense (500 trees/ha).

Previous, blind strategies that sample based on pre-defined waypoints (i.e., sequentially with a single camera drone or parallelly with camera arrays) were reconsidered in the experiment shown in Fig. 2. While brute-force sequential sampling led to a



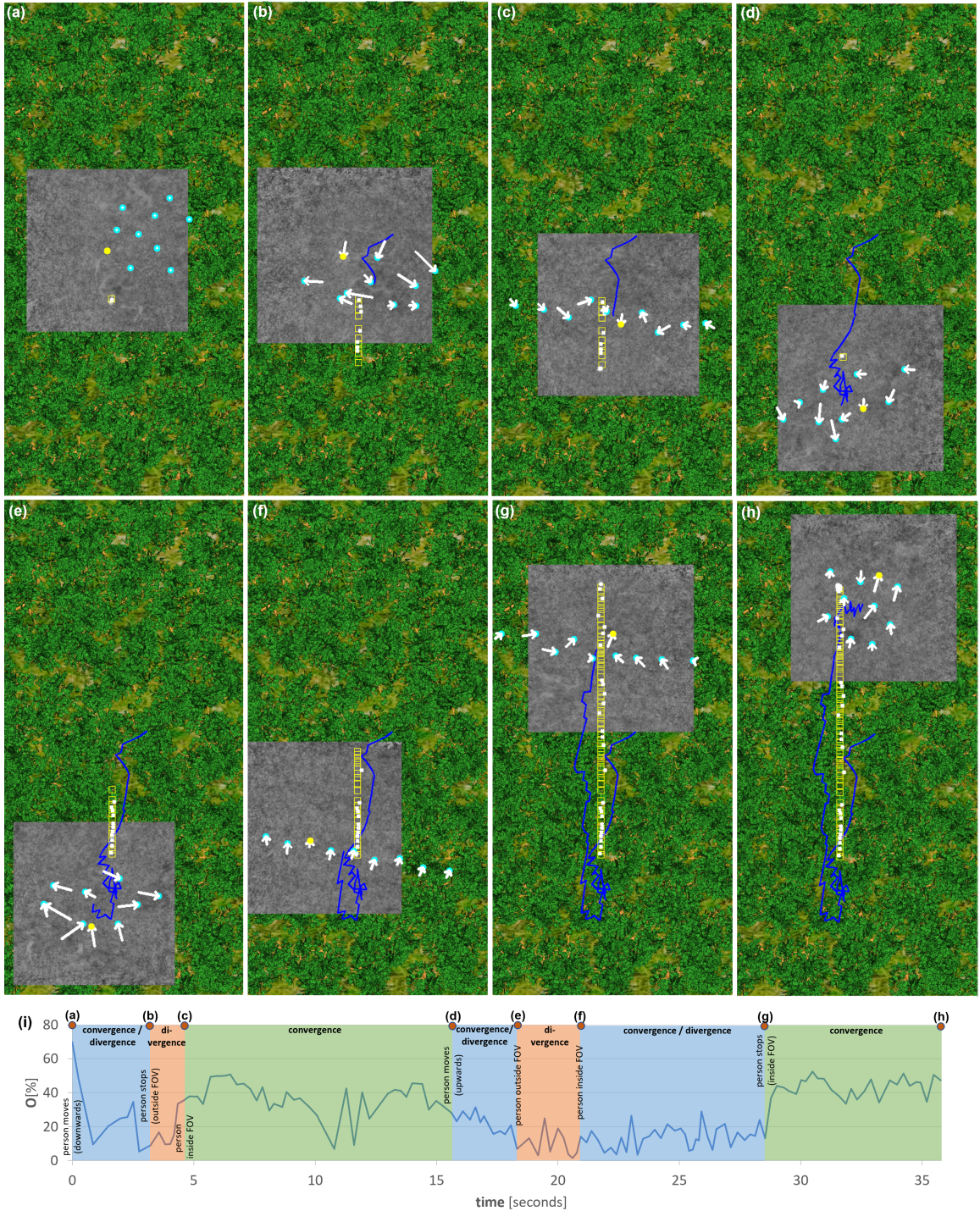


**Fig. 5** Starting from the final state shown in Fig. 3 (a), a walking person (speed:  $4 \text{ m/s}$ ) was simulated: moving  $13 \text{ m}$  downwards (a-b), resting for  $12 \text{ s}$  (b-d), moving  $55 \text{ m}$  upwards (d-g), resting (g-h). The target visibility while the swarm is tracking the person is shown in (i), and the different convergence and divergence phases of the swarm are highlighted. Note that the yellow boxes highlight the target's ground-truth positions, the white stars indicate the target's estimated positions, the white arrows show the movement of the drones between time steps  $t-1$  and  $t$ , the blue lines represent the total sampling paths of the swarm's center of gravity, the yellow dots indicate the best sampling position at time  $t$ , and the grey area shows the integrated ground coverage at time  $t$ . Simulation parameters (see **Methods** for details): drones' ground speed =  $10 \text{ m/s}$ ,  $\Delta_h = 1 \text{ m}$ , forest density =  $300 \text{ trees/ha}$ ,  $n = 10$ ,  $T = 16.3\%$ ,  $h_1 = 35 \text{ m}$ ,  $c_1 = 1 \text{ m}$ ,  $c_2 = 2 \text{ m}$ ,  $c_3 = 1.643 \text{ m}$ ,  $s = c_4 = 4.2 \text{ m}$ ,  $c_5 = 0.3$ . See Supplementary Video 5.

relatively high visibility improvement through occlusion removal after a relatively long time (51% *MTV* after 75 seconds), parallel sampling resulted very quickly with only marginal visibility improvements (19% *MTV* after 3 seconds). In both cases, local occlusion densities of the forest or view obliqueness of the target were not considered. Note that the geometric distribution behaviour of visibility improvement that can be observed for sequential sampling with an increasing number of integrated images matches the findings made with the statistical model described in [77].

Adaptively sampling drone swarms that consider local occlusion density and target view obliqueness, however, can significantly increase visibility while reducing sampling time, as shown in the next experiment (Fig. 3). Under the same conditions as for the experiments in Fig. 2, an *MTV* of 72% was reached after 14 seconds because the swarm found and converged over gaps or sparse density regions in the vegetation while preferring oblique target views. Our PSO that guides the swarm behaviour considers sequentially as well as parallelly captured samples for maximizing target visibility, as explained in detail in **Methods**.

The size of the swarm clearly matters, as shown in the experiment in Fig. 4 (a-c,f). Larger swarms profit from a wider SA and a denser sampling. They consequently led to better visibility (max. 72% for  $n = 10$ , 35% for  $n = 5$ , and 22% for  $n = 3$ ) and larger sampling coverage.

With increasing forest density, visibility decreases because of denser occlusion, as can be seen in the experiment in Fig. 4(c-e,g). By repeating the experiment shown in Fig. 3, *MTV* drops from 72% (300trees/ha) down to 42% (400trees/ha) and 31% (500trees/ha).

Moving targets can also be detected and tracked. For the experiment shown in Fig. 5, the average differences between the target's ground truth position, motion speed, motion direction and the corresponding estimations of our PSO were 0.59 m, 0.09 m/s, and 9.21 /circ, respectively. When the target leaves the swarm's view, the swarm starts to diverge into the default scanning pattern towards the last known target position. When the target stops, the swarm mainly converges into a circular SA pattern. If the target is inside the swarm's view while moving, the swarm converges and diverges depending on the local occlusion situation. This is illustrated in Fig. 5(i). **S3** of the

supplementary material presents a further motion example.

A detailed discussion of these results is provided in **Discussion and Conclusion**.

## Methods

### Particle Swarm Optimization

In order to determine the particle positions at time  $t + 1$ , classical POS algorithms [85–92] add the following velocity vectors to the current positions at time instance  $t$ :

$$V_i^{t+1} = c_0 \cdot (V_i^t) + c_1 \cdot r_1 (P_{\text{best}}^i - P_i^t) + c_2 \cdot r_2 (G_{\text{best}} - P_i^t), \quad (1)$$

where  $P_{\text{best}}^i$  is the position of best objective ever explored by particle  $i$ ,  $G_{\text{best}}$  is the position of the best objective ever explored by any particle,  $r_1$  and  $r_2$  are random numbers ( $0 \dots 1$ ), and  $c_0$ ,  $c_1$ ,  $c_2$  are the hyper-parameters. Here,  $c_0$  is the inertia weight constant (i.e., how much of the previous velocity is preserved),  $c_1$  is the cognitive coefficient, which refines the results of each particle, and  $c_2$  is the social coefficient, which refines the results of the entire swarm.

For our problem, two main observations can be made:

(1) Our objective function is based on randomness (forest occlusion) and is (especially in the case of target motion) not constant. It is neither linear nor smooth, and certainly not differentiable. The latter is the reason for choosing PSO in general, as gradient-decent-based optimizations are not possible.

(2) A bias towards the positions with the best sample values over history (either for a single particle  $P_{\text{best}}^i$  or for the global swarm  $G_{\text{best}}$ ) is not effective if dynamics and randomness affect the objective function. Sampling multiple times at the same (best) position does not improve the objective in our case, as no additional unoccluded parts of the target can possibly be seen. Therefore, particles must always remain dynamic in our case (and not converge to a single position), and must cover the SA effectively.

To address these two observations, our PSO approach must be much more explorative than exploitative:



(1) The swarm behaviour itself is constrained to the current time instance (i.e., not considering history): random local explorations of particles with a bias towards a temporal global leader (i.e., the best sample at the current time instance), enforcing a minimal distance constraint that defines the SA properties.

(2) The objective function is conditionally integrated (i.e., a new sample is integrated only if it improves the objective), using parallel samples (i.e., samples taken at the current time instance) and sequential samples (i.e., samples taken at previous time instances).

(3) Instead of an inertia weight constant, we apply a condition (i.e., if nothing is found) bias towards a default scanning pattern.

Algorithm 1 summarizes one iteration of our PSO approach at time instance  $t$ .

---

#### Algorithm 1 PSO Iteration

---

**Require:** at time  $t$  drone  $i$  is at position  $P_i^t$

**Ensure:**  $\tilde{I}_{\text{best}}^t$  has highest  $O$  from  $P_{\text{best}}^t$

```

1: if  $O(\tilde{I}_{\text{best}}^t) < T$  then
2:    $L^t = \text{line}(P^t, SD, s), s \geq c_4$ 
3:    $V_i^{t+1} = c_3 \cdot SD + c_5 \cdot (L_i^t - P_i^t)$ 
4:    $P_i^{t+1} = P_i^t + V_i^{t+1}$ 
5: else
6:    $\tilde{I}_{\text{best}}^t = \sum_{i,t} (I_i^t)$  from  $P_{\text{best}}^t$ 1
7:    $V_i^{t+1} = c_1 \cdot \text{norm}(R) + c_2 \cdot \text{norm}(P_{\text{best}}^t - P_i^t)$ 
8:    $P_i^{t+1} = \text{Rutherford}(P_i^t + V_i^{t+1}, c_4)$ 
9:   update  $SD, c_3$  wrt. target appearance
10: end if

```

---

It requires five hyper-parameters that are discussed in more detail in **Hyper-Parameters**:  $c_1$  is the cognitive coefficient, which refines each particle's position randomly,  $c_2$  is the social coefficient, which refines the position of the entire swarm towards the best sampling position ( $P_{\text{best}}^t$ , indicated in yellow in Figs. 3 - 5) at time instance  $t$ ,  $c_3$  is the scanning speed of the swarm if nothing is found (i.e., for the default scanning pattern),  $c_4$  is the minimal sampling distance (minimal horizontal distance of drones), and  $c_5$  (0..1) is the speed of particles' divergence back towards the default scanning pattern if the target is lost. Note that  $R$  is a random

vector, and that positions and velocities are in 2D (defined on the horizontal scanning plane that is parallel to the ground plane).

Lines 1-4 implement our conditioned bias towards a default scanning pattern if nothing is found or a previously found target is lost. Our default scanning pattern (defined by the function *lines* and stored in  $L^t$ ) is linear (i.e., all drones in a line) and centered at the center of gravity of all drone positions ( $P^t$ ) at time instance  $t$ , spaced at distance  $s \geq c_4$ , and moving at speed  $c_3$  along the scanning direction  $SD$ . A linear scanning configuration moving in perpendicular direction ensures the widest ground coverage. As for single drones, scanning direction and speed can be defined by waypoints. The speed of divergence towards the default scanning pattern if a target is lost is  $c_5$  (0..1).

Lines 5-10 implement the convergence of the swarm if a potential target is detected. In this case, the best integral image ( $\tilde{I}_{\text{best}}^t$ ) is computed for the best sampling position ( $P_{\text{best}}^t$ ) at time  $t$  by integrating (i.e., registering to  $P_{\text{best}}^t$  and summing) all single images ( $I_i^t$ ) captured by all drones ( $i$ ) at all sampling times ( $t$ ) only if integrating  $I_i^t$  improves our objective (i.e., increases visibility in  $\tilde{I}_{\text{best}}^t$ ). We then determine the velocities  $V_i^{t+1}$  for the next time instance  $t + 1$  by our cognitive ( $c_1$ ) and social ( $c_2$ ) components. These velocities are applied to determine the next sample positions  $P_i^{t+1}$ . The minimal distance ( $c_4$ ) constraint is enforced by Rutherford scattering [93]. Finally, the direction ( $SD$ ) and speed ( $c_3$ ) of the default scanning pattern are updated with respect to the detected target appearance (i.e., its position and motion speed/direction). Position and motion parameters can be computed from two consecutive iterations where the target was detected.  $SD$  is the normalized vector between the most recent target position and the swarm's center of gravity at that time, and  $c_3$  is the distance by which the target moves during the iteration time (i.e., duration of the most recent iteration) plus some delta which guarantees that the swarm can keep pace with the target (i.e., the swarm is faster than the target). The updated  $SD$  and  $c_3$  become effective when the target is lost. In this case, the swarm diverges at appropriate speed towards the default scanning pattern in the direction of the most recent target appearance.

Our objective function ( $O$ ) is explained in detail in **Objective Function**. Its result is compared to a

---

<sup>1</sup> Integrate  $I_i^t$  only if it improves objective.

defined limit ( $T$ ) for distinguishing a potential target signal from false positives. Note that we repeat our POS iterations until, for example, the objective is high enough to clearly indicate a finding or the process is aborted manually. More details are presented in the following sections.

## Collision Avoidance

For simple collision avoidance, we operate the drones at various altitudes with uniform height differences of  $\Delta h$ . Thus, the maximum height difference between the highest and the lowest drone is  $\Delta h_{\max} = \Delta h \cdot n$  for  $n$  drones in the swarm. Although different sampling altitudes lead to variations in spatial sampling resolution on the ground, this has almost no effect in our integral images.

The ground coverage of a drone depends on the field of view ( $fov$ ) of its camera [80], and is:

$$c_l = \left( 2 \cdot h_l \cdot \tan \left( \frac{fov}{2} \right) \right)^2 \quad (2)$$

for the lowest, and

$$c_h = \left( 2 \cdot (h_l + \Delta h \cdot n) \cdot \tan \left( \frac{fov}{2} \right) \right)^2 \quad (3)$$

for the highest drone. The average coverage in the integral image is therefore:

$$c_{avg} = \left( 2 \cdot \tan \left( \frac{fov}{2} \right) \right)^2 \cdot \left( h_l^2 + (h_l \cdot \Delta h \cdot (n-1)) + \Delta h^2 \frac{2n^2 - 3n - 1}{6} \right). \quad (4)$$

The corresponding spatial sampling loss ratio due to height differences is:

$$SL_{\Delta h} = \frac{c_{avg}}{c_l} = 1 + \left( \frac{\Delta h}{h_l} \right)^2 \cdot \left( \frac{2n^2 - 3n + 1}{6} \right) + \left( \frac{\Delta h}{h_l} \right) \cdot (n-1). \quad (5)$$

The coverage of a single pixel on the ground is (for the lowest and highest drone, respectively):

$$c_{pxl} = \frac{c_l}{px}, \quad (6)$$

$$c_{pxh} = \frac{c_h}{px}. \quad (7)$$

The spatial sampling loss ratio due to pose estimation error  $e$  [77] is:

$$SL_e = 1 + \frac{4e^2 + 4e \cdot \sqrt{c_{pxl}}}{c_{pxl}}. \quad (8)$$

Consequently, the total spatial sampling loss ratio is:

$$SL = SL_e \cdot SL_{\Delta h}. \quad (9)$$

To avoid that drones at higher altitudes capture images of drones at lower altitudes, the maximum height difference and the vertical spacing of the drones depend on the the minimal horizontal sampling distance ( $c_4$ ) and the cameras' field of view ( $fov$ ):

$$c_4 = \Delta h_{\max} \cdot \tan \left( \frac{fov}{2} \right) = \Delta h \cdot (n-1) \cdot \tan \left( \frac{fov}{2} \right), \quad (10)$$

where  $n$  neighbouring drones are vertically separated by  $\Delta h$ .

Assuming realistic parameters, for example,  $\Delta h = 1 \text{ m}$ ,  $n = 10$ ,  $fov = 50^\circ$ ,  $h_l = 35 \text{ m}$ ,  $p_x = 512 \times 512 \text{ pixels}$ ,  $e = 0.05 \text{ m}$  (for RTK based GPS precision), would make the spatial sampling resolution drop from  $6 \times 6 \text{ pixels/m}^2$  (sampling at the same altitude) to  $5 \times 5 \text{ pixels/m}^2$  (sampling at different altitudes) – both including the reduction in spatial sampling resolution due to the pose estimation error, as discussed in [77]. Here,  $SL_{\Delta h} = 1.28$ ,  $SL_e = 6.57$ ,  $SL = 8.4$ , and  $c_4 = 4.19 \text{ m}$ .

This example illustrates that, compared to sampling at the same altitude, sampling at different altitudes has a minimal impact on the spatial sampling resolution of integral images. This is due not only to the integration itself (where multiple spatial sampling resolutions are combined in case they are sampled from different altitudes), but also to slight misregistrations (due to pose estimation errors) being much more dominant than resolution differences (compare  $SL_{\Delta h}$  with  $SL_e$  above).

A comparison of integral images sampled at different altitudes and at the same altitude is shown in **S2** of the supplementary material.

Note that the altitude differences for our default (linear) scanning pattern, as explained in **Particle Swarm Optimization**, were chosen to alternate equally over space as follows: highest, third-highest, fifth-highest, etc. altitude from the outer-most position of one side inwards, and second-highest, fourth-highest, sixth-highest, etc. altitude from the outer-most position of the opposite side inwards. This maximizes the overlapping ground coverage [80].

## Objective Function

If the swarm consist of  $n$  drones that sample over  $\tau$  time instances, we capture a total of  $n \cdot \tau$  single images. At each time instance  $t$ ,  $n$  images are captured in parallel, while  $n$ -tuples of parallel samples are captured sequentially over  $\tau$  steps.

To compute, the integral image, we first apply a Reed-Xiaoli (RX) anomaly detector [94] to the  $n$  latest single images captured at the current time instance  $t$  to detect pixels that are abnormal with respect to the background statistics. Note that all images captured contain four spectral bands (cf. Fig. 3b): red, green, blue, far infrared/thermal. Consequently, we detect anomalies in color and temperature, which has proven to be more efficient than color anomaly detection or thermal anomaly detection alone [95].

We then integrate the masked results (i.e., binarized after anomaly score thresholding) to cope with different amounts of image overlap during swarm sampling, using a constant anomaly-score threshold (i.e., 0.9998 = 99.98% in all our experiments). The registration of these images is relative to one of the  $n$  perspectives. Without occlusion, the choice of the reference perspective is irrelevant, as the target's footprint would only shift to different pixel positions in the integral image for each reference perspective, but would not change otherwise. With occlusion, however, we can gain more visibility from some reference perspectives than from others due to varying visibility from different perspectives. Therefore, we determine the best integral  $\tilde{I}_{\text{best}}^t$  with the highest  $O(\cdot)$  and its corresponding reference pose  $P_{\text{best}}^t$ .

Once  $P_{\text{best}}^t$  is known, all single images captured at previous time steps are also anomaly-masked

and integrated to  $\tilde{I}_{\text{best}}^t$  for  $P_{\text{best}}^t$  – but only if they improve the objective (i.e., if they enhance visibility and in the case of  $f_{ov}$  overlap - which indicates overlapping coverage on the ground). Finally, we remove previously integrated single images of the  $n$ -latest set from  $\tilde{I}_{\text{best}}^t$  if this also leads to an improvement of our objective.

Note that  $\tilde{I}_{\text{best}}^t$ ,  $P_{\text{best}}^t$ , and  $objective(\tilde{I}_{\text{best}}^t)$  are required for our PSO interaction (algorithm 1, lines 1,6, and 7).

Our hypothesis is that visibility of the target improves with more integrated samples [77]. In the absence of occlusion, for instance, the target should appear fully visible in the integral image, and its projected pixel footprint should have the maximum size from oblique viewing angles. However, this footprint is reduced with increasing occlusion, as only fractions of it might be reconstructable (i.e., parts that are fully occluded in all or most samples will remain invisible). It is also reduced by less oblique viewing angles.

Therefore, our  $O(\tilde{I}_{\text{best}}^t)$  function determines the contour size of the largest connected pixel cluster (i.e., blob, cf. Fig. 3b) among the abnormal pixels detected and integrated in  $\tilde{I}_{\text{best}}^t$ , using the raster chain tree algorithm [96]. This contour size is our objective score. According to our hypothesis, it grows with improving visibility.

The center of gravity of the blob contour represents the estimated target position.

## Hyper-Parameters

After convergence due to a potential finding, our PSO iterations approximate a solution to the *packing circles in a circle* problem [97], as illustrated in Fig. 6.

Here, the inner circles represent the possible locations of each drone at time instance  $t$ , while the outer circle represents the SA area being sampled. To guarantee the minimal horizontal search distance, it follows that  $c_1 + c_2 \leq c_4$ . To avoid that the cognitive search behaviour of the swarm overrules its social search behaviour, it follows that  $c_1 \leq c_2$ .

The sampling rate in the default scanning direction is defined by  $c_3$  (i.e., images in the default scanning direction are taken every  $c_3$  meters). After a target has been detected,  $c_3$  should be chosen to be larger than the distance the target can move during

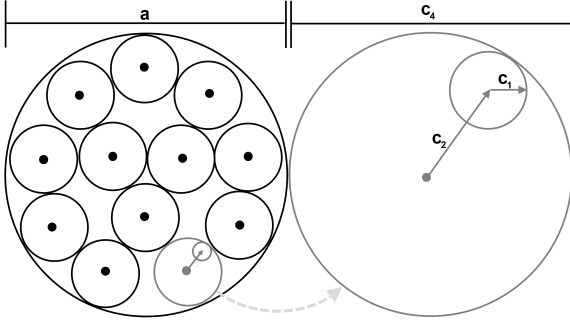


**Fig. 6** PSO's approximation to a *packing circles in a circle* solution: The possible movement of each drone in one PSO iteration is  $c_1 + c_2$ , and must be less than or equal to the minimal horizontal search distance  $c_4$ .

the iteration time (which can be determined automatically), as explained in **Particle Swarm Optimization**). Note that  $s \geq c_4$  represents the sampling rate in the orthogonal direction. The smoothness of the divergence towards the default sampling pattern after the target has been lost is controlled by  $c_5$  (0..1). The larger, the quicker the divergence. Low values (e.g., 0.3 = 30%) should be chosen for smooth transitions.

Note that the iteration time varies, as it equals the required duration of the drone with the longest travel distance to reach its position. To avoid over-sampling,  $c_2 - c_1$  (which is the smallest possible distance a drone can move in each iteration) must not be less than the minimum sampling baseline, which depends on projected occluder sizes, as explained in [77].

Finally, the diameter  $a$  of the SA is  $a = c_4 \cdot r_n$ , where  $r_n$  is the packing number [98–104] for  $n$  circles (i.e., drones) of the the *packing circles in a circle* problem [97]. For example, the SA diameter for  $n = 10$  drones at minimal horizontal sampling distance of  $c_4 = 4.19\text{ m}$  is  $15.976\text{ m}$ , as  $r_{10} = 3.813$ .

## Implementation

Our forest simulation<sup>2</sup> was realized with a procedural tree algorithm called *ProcTree*<sup>3</sup> and was implemented with WebGL. For all our experiments, it computed  $p_x = 512 \times 512$  *pixels* aerial images (RGB and thermal) for drone flights over a pre-defined area and for defined sampling parameters (e.g., waypoints, altitudes, and camera field of view).

The virtual rendering camera ( $fov = 50^\circ$  in our case) applied perspective projection and was aligned with its look-at vector parallel to the ground surface normal (i.e., pointing downwards). Procedural tree parameters, such as tree height (20 m – 25 m), trunk length (4 m – 8 m), trunk radius (20 cm – 50 cm), and leaf size (5 cm – 20 cm) were used to generate a representative mixture of broadleaf tree species. Finally, a seeded random generator was applied to generate a variety of trees at defined densities and degrees of similarity. Environmental properties, such as tree species, foliage and time of year, were assumed to be constant, as we were interested mainly in effects caused by changing sampling parameters. Forest density was considered sparse with 300 *trees/ha*, medium with 400 *trees/ha*, and dense with 500 *trees/ha*.

Simulated integral images are compared with integral images captured over real forest in S1 of the supplementary material.

## Discussion and Conclusion

In all our experiments, the target was found at the correct position if it was detected. The chances for a detection, however, were generally much lower in the case of blind uniform sampling (parallel or sequential) than for adaptive sampling of a swarm (e.g.,  $3.8 \times / 1.4 \times$  for blind parallel/sequential sampling, cf. Figs. 2,3). Swarm sampling reached a particular target visibility significantly faster than blind-brute force sequential sampling (e.g.,  $12 \times$  to reach an *MTV* of at least 50%, cf. Figs. 2,3), while blind parallel sampling was fast but never achieved adequate target visibility.

The reason why swarms significantly outperform blind sampling strategies in terms of performance and detection rate is that sampling can be adapted autonomously to locally sparser forest regions and to larger target view obliqueness. In all our experiments swarms preferred to converge at certain distances from the target (rather than directly above it) to maximize target view obliqueness. In open fields this would be the only possibility to improve visibility, as it increases the projected footprint of the target. In occluding forests, however, sampling through locally sparse regions is another factor to be considered. Our PSO and objective function optimize for both (sparseness and obliqueness) while also combining sequentially and parallelly recorded samples whenever possible.

<sup>2</sup>Source Code: <https://github.com/JKU-ICG/AOS> (AOS for Drone Swarms)

<sup>3</sup>Source Code: <https://github.com/supereggbert/proctree.js>

The wider SA and denser sampling of larger swarms will always lead to better visibility, larger coverage, and consequently to a higher detection probability, as shown in Fig. 4(a-c,f). Stronger occlusion will generally reduce visibility, as illustrated by Fig. 4(c-e,g).

For static targets, visibility increases with the number ( $N$ ) of images being integrated. Under the assumption of uniformity (size and distribution of occluders), the following statistical behaviour describes the visibility ( $V$ ) of a target in an image where occlusion appears with density ( $D$ ) [77]:

$$V = 1 - D^2 - \left( \frac{D(1-D)}{N} \right). \quad (11)$$

Visibility improvement has upper and lower limits that depend on  $D$ . In the worst case, with a single image ( $N = 1$ ):  $V_{min} = 1 - D$ . In the best case, with an infinite number of images being integrated ( $N = \infty$ ):  $V_{max} = 1 - D^2$ . Note that in the case of non-uniform occlusion volumes that are uniformly sampled, the same principle applies under the assumption that  $D$  is the average density over the  $N$  samples. This can be observed for the blind brute-force sequential sampling shown in Fig. 2(d), where  $N$  was sufficiently large. It reveals the same geometric distribution behaviour as for uniform occlusion volumes [77]. For non-uniform occlusion volumes which are adaptively sampled, as in the case of our drone swarms and PSO, the density of each sample cannot be considered statistically equal, as it is minimized individually. For this reason,  $V$  increases much quicker and settles at much higher value than in blind sampling, as shown in Fig. 3(e).

For moving targets, integrating images captured at previous time steps does not improve visibility if the projection of the target does not overlap with its projection in the most recent recordings. In this case, they are not integrated (see line 6 of algorithm 1), and only the most recent samples that are captured parallelly at the current time step can contribute to occlusion removal. Consequently, target visibility drops during motion, and increases again when the target stops, as illustrated in Fig. 5(i). Although moving targets were detected and tracked reliably in our experiments, they can be lost if they remain in excessively dense regions for too long or if they move too fast (i.e., faster than the swarm can follow). Section S4 of the supplementary material extends the statistical visibility model for uniform

occlusion volumes and static targets (Eqn. 11, [77]) to include parallel-sequential sampling in the presence of moving targets (Eqn. S15). It also considers the contribution to visibility improvement of overlapping target projections in sequential samples, depending on target and drone speeds. As for static targets, this model is also outperformed in adaptive sampling of moving targets in non-uniform occlusion volumes due to the individual view optimization of the PSO.

With our centralized implementation running on a consumer PC (i5-4570 CPU, 3.20GHz, 24 GB RAM), we achieved an average (not performance-optimized) processing time for each PSO iteration of 96 ms for each of the  $n$  latest (i.e., parallelly captured) samples, and 30 ms for each of the  $n \cdot \tau$  samples captured during the  $\tau$  previous (i.e., sequential) time steps. For  $n = 10$  and by limiting  $\tau$  to 3, for example, one PSO iteration requires 960 ms + 900 ms = 1.86 s and processes a total of 40 images. With a decentralized implementation, image capturing and transmission as well as anomaly detection can be carried out in parallel on each drone. Faster GPU implementations of the anomaly detector lead to an additional speed-up.

Our simulation differs from the real world: Acceleration and deceleration of drones, data transmission times (e.g., images and waypoints), and errors of sensors (e.g., GPS imprecision and camera noise) are not considered. Compared to a real forest, our procedural forest is simplified. Although this influences performance and quality, it does not affect our finding that swarms significantly outperform blind sampling in performance and detection rate under same conditions. We plan to experiment with physical drone swarms in real environments in the future.

The threshold  $T$  that is needed by our PSO (see line 1 of algorithm 1) for outlier removal was always set to be slightly higher than the largest false-positive blob detected when the target is not in view. To determine it, several representative sample sets without target were considered. Automatic and adaptive determination of this threshold will be part of future work.

Our collision avoidance strategy is simple, but effective for AOS. It requires neither a computational nor a communication effort. Alternatives that have the potential to reduce the minimal sampling distance  $c_4$  further need to be investigated. A smaller  $c_4$  leads to shorter flight distances of



individual drones during each PSO iteration, and consequently to faster reaction times of the whole swarm. Wider SAs and denser sampling can always be achieved with larger swarms.

Finally, we believe that ongoing and rapid technological development will make large drones swarms feasible, affordable, and effective in the near future – not only for military but, in particular, also for civil applications, such as search and rescue. For other synthetic aperture imaging applications that go beyond occlusion removal, drone swarms have the potential to become an ideal tool for realizing dynamic sampling of adaptive wide-aperture lens optics in remote sensing scenarios.

## References

- [1] Chung, S.-J., Paranjape, A. A., Dames, P., Shen, S. & Kumar, V. A survey on aerial swarm robotics. *IEEE Transactions on Robotics* **34** (4), 837–855 (2018) .
- [2] Coppola, M., McGuire, K. N., De Wagter, C. & De Croon, G. C. A survey on swarming with micro air vehicles: Fundamental challenges and constraints. *Frontiers in Robotics and AI* **7**, 18 (2020) .
- [3] Zhou, Y., Rao, B. & Wang, W. Uav swarm intelligence: Recent advances and future trends. *IEEE Access* **8**, 183856–183878 (2020) .
- [4] Abdelkader, M., Güler, S., Jaleel, H. & Shamma, J. S. Aerial swarms: Recent applications and challenges. *Current Robotics Reports* **2** (3), 309–320 (2021) .
- [5] Tang, J., Duan, H. & Lao, S. Swarm intelligence algorithms for multiple unmanned aerial vehicles collaboration: A comprehensive review. *Artificial Intelligence Review* 1–33 (2022) .
- [6] Saska, M. *et al.* Swarm distribution and deployment for cooperative surveillance by micro-aerial vehicles. *Journal of Intelligent & Robotic Systems* **84** (1), 469–492 (2016) .
- [7] Chriki, A., Touati, H., Snoussi, H. & Kamoun, F. *Uav-gcs centralized data-oriented communication architecture for crowd surveillance applications*, 2064–2069 (IEEE, 2019).
- [8] Scaramuzza, D. *et al.* Vision-controlled micro flying robots: from system design to autonomous navigation and mapping in gps-denied environments. *IEEE Robotics & Automation Magazine* **21** (3), 26–40 (2014) .
- [9] Abdelkader, M., Lu, Y., Jaleel, H. & Shamma, J. S. *Distributed real time control of multiple uavs in adversarial environment: Algorithm and flight testing results*, 6659–6664 (IEEE, 2018).
- [10] Scherer, J. & Rinner, B. Multi-uav surveillance with minimum information idleness and latency constraints. *IEEE Robotics and Automation Letters* **5** (3), 4812–4819 (2020) .
- [11] Spry, S. C., Girard, A. R. & Hedrick, J. K. *Convoy protection using multiple unmanned aerial vehicles: organization and coordination*, 3524–3529 (IEEE, 2005).
- [12] Ding, X. C., Rahmani, A. R. & Egerstedt, M. Multi-uav convoy protection: An optimal approach to path planning and coordination. *IEEE transactions on Robotics* **26** (2), 256–268 (2010) .
- [13] Fu, Z., Chen, Y., Ding, Y. & He, D. Pollution source localization based on multi-uav cooperative communication. *IEEE Access* **7**, 29304–29312 (2019) .
- [14] Hayajneh, A. M., Zaidi, S. A. R., McLernon, D. C. & Ghogho, M. *Drone empowered small cellular disaster recovery networks for resilient smart cities*, 1–6 (IEEE, 2016).
- [15] Fotouhi, A. *et al.* Survey on uav cellular communications: Practical aspects, standardization advancements, regulation, and security challenges. *IEEE Communications surveys & tutorials* **21** (4), 3417–3442 (2019) .
- [16] Arafat, M. Y. & Moh, S. A survey on cluster-based routing protocols for unmanned aerial vehicle networks. *IEEE Access* **7**, 498–516 (2018) .

- [17] Fu, S. *et al.* Joint unmanned aerial vehicle (uav) deployment and power control for internet of things networks. *IEEE Transactions on Vehicular Technology* **69** (4), 4367–4378 (2020) .
- [18] Kravchuk, S. O., Kaidenko, M. M. & Kravchuk, I. M. *Experimental development of communication services scenario for centralized and distributed construction of a collective control network for drone swarm*, 21–24 (IEEE, 2021).
- [19] Sa, I. & Corke, P. *Vertical infrastructure inspection using a quadcopter and shared autonomy control*, 219–232 (Springer, 2014).
- [20] Lindsey, Q., Mellinger, D. & Kumar, V. Construction with quadrotor teams. *Autonomous Robots* **33** (3), 323–336 (2012) .
- [21] Augugliaro, F. *et al.* The flight assembled architecture installation: Cooperative construction with flying machines. *IEEE Control Systems Magazine* **34** (4), 46–64 (2014) .
- [22] Palunko, I., Fierro, R. & Cruz, P. *Trajectory generation for swing-free maneuvers of a quadrotor with suspended payload: A dynamic programming approach*, 2691–2697 (IEEE, 2012).
- [23] Alexis, K., Nikolakopoulos, G., Tzes, A. & Dritsas, L. in *Coordination of helicopter uavs for aerial forest-fire surveillance* 169–193 (Springer, 2009).
- [24] Achtelik, M. *et al.* *Sfly: Swarm of micro flying robots*, 2649–2650 (IEEE, 2012).
- [25] Zhou, X. *et al.* Swarm of micro flying robots in the wild. *Science Robotics* **7** (66), eabm5954 (2022) .
- [26] Schedl, D. C., Kurmi, I. & Bimber, O. Search and rescue with airborne optical sectioning. *Nature Machine Intelligence* **2** (12), 783–790 (2020) .
- [27] Schedl, D. C., Kurmi, I. & Bimber, O. An autonomous drone for search and rescue in forests using airborne optical sectioning. *Science Robotics* **6** (55), eabg1188 (2021) .
- [28] Amala Arokia Nathan, R. J., Kurmi, I., Schedl, D. C. & Bimber, O. Through-foliage tracking with airborne optical sectioning. *Journal of Remote Sensing* **2022** (2022) .
- [29] Oh, K.-K., Park, M.-C. & Ahn, H.-S. A survey of multi-agent formation control. *Automatica* **53**, 424–440 (2015) .
- [30] Saska, M., Vakula, J. & Přeucil, L. *Swarms of micro aerial vehicles stabilized under a visual relative localization*, 3570–3575 (IEEE, 2014).
- [31] Saska, M. *Mav-swarms: unmanned aerial vehicles stabilized along a given path using onboard relative localization*, 894–903 (IEEE, 2015).
- [32] Vásárhelyi, G. *et al.* Optimized flocking of autonomous drones in confined environments. *Science Robotics* **3** (20), eaat3536 (2018) .
- [33] McGuire, K., De Wagter, C., Tuyls, K., Kappen, H. & de Croon, G. C. Minimal navigation solution for a swarm of tiny flying robots to explore an unknown environment. *Science Robotics* **4** (35), eaaw9710 (2019) .
- [34] Spurný, V. *et al.* Cooperative autonomous search, grasping, and delivering in a treasure hunt scenario by a team of unmanned aerial vehicles. *Journal of Field Robotics* **36** (1), 125–148 (2019) .
- [35] Ramirez-Atencia, C., Camacho, D. *et al.* Handling swarm of uavs based on evolutionary multi-objective optimization. *Progress in Artificial Intelligence* **6** (3), 263–274 (2017) .
- [36] Zhen, Z., Xing, D. & Gao, C. Cooperative search-attack mission planning for multi-uav based on intelligent self-organized algorithm. *Aerospace Science and Technology* **76**, 402–411 (2018) .
- [37] Wilhelm, J., Rojas, J., Eberhart, G. & Perhinschi, M. Heterogeneous aerial platform adaptive mission planning using genetic algorithms. *Unmanned Systems* **5** (01), 19–30 (2017) .

- [38] Zhao, W., Meng, Q. & Chung, P. W. A heuristic distributed task allocation method for multivehicle multitask problems and its application to search and rescue scenario. *IEEE transactions on cybernetics* **46** (4), 902–915 (2015).
- [39] Alotaibi, E. T., Alqefari, S. S. & Koubaa, A. Lsar: Multi-uav collaboration for search and rescue missions. *IEEE Access* **7**, 55817–55832 (2019).
- [40] Wang, H., Cao, M., Jiang, H. & Xie, L. *Feasible computationally efficient path planning for uav collision avoidance*, 576–581 (IEEE, 2018).
- [41] Theile, M., Bayerlein, H., Nai, R., Gesbert, D. & Caccamo, M. *Uav coverage path planning under varying power constraints using deep reinforcement learning*, 1444–1449 (IEEE, 2020).
- [42] Brambilla, M., Ferrante, E., Birattari, M. & Dorigo, M. Swarm robotics: a review from the swarm engineering perspective. *Swarm Intelligence* **7** (1), 1–41 (2013).
- [43] Bredeche, N., Haasdijk, E. & Prieto, A. Embodied evolution in collective robotics: a review. *Frontiers in Robotics and AI* **5**, 12 (2018).
- [44] Lee, K.-B., Kim, Y.-J. & Hong, Y.-D. Real-time swarm search method for real-world quadcopter drones. *Applied Sciences* **8** (7), 1169 (2018).
- [45] Jatmiko, W., Sekiyama, K. & Fukuda, T. Modified particle swarm robotic for odor source localization in dynamic environment. *The International Journal of Intelligent Control and Systems: Special Issue on Swarm Robotic* **11** (3), 176–184 (2006).
- [46] Turduev, M., Ataş, Y., Sousa, P., Gazi, V. & Marques, L. *Cooperative chemical concentration map building using decentralized asynchronous particle swarm optimization based search by mobile robots*, 4175–4180 (IEEE, 2010).
- [47] Jatmiko, W. *et al.* *Localizing multiple odor sources in dynamic environment using ranged subgroup pso with flow of wind based on open dynamic engine library*, 602–607 (IEEE, 2009).
- [48] Jatmiko, W., Sekiyama, K. & Fukuda, T. A pso-based mobile robot for odor source localization in dynamic advection-diffusion with obstacles environment: theory, simulation and measurement. *IEEE Computational Intelligence Magazine* **2** (2), 37–51 (2007).
- [49] Ferri, G. *et al.* *Explorative particle swarm optimization method for gas/odor source localization in an indoor environment with no strong airflow*, 841–846 (IEEE, 2007).
- [50] Steiner, J. A., Bourne, J. R., He, X., Cropek, D. M. & Leang, K. K. *Chemical-source localization using a swarm of decentralized unmanned aerial vehicles for urban/suburban environments*, Vol. 59162, V003T21A006 (American Society of Mechanical Engineers, 2019).
- [51] Zhen, X., Enze, Z. & Qingwei, C. Rotary unmanned aerial vehicles path planning in rough terrain based on multi-objective particle swarm optimization. *Journal of Systems Engineering and Electronics* **31** (1), 130–141 (2020).
- [52] Ali, Z. A. & Zhangang, H. Multi-unmanned aerial vehicle swarm formation control using hybrid strategy. *Transactions of the Institute of Measurement and Control* **43** (12), 2689–2701 (2021).
- [53] Hoang, V. T., Phung, M. D., Dinh, T. H., Zhu, Q. & Ha, Q. P. *Reconfigurable multi-uav formation using angle-encoded pso*, 1670–1675 (IEEE, 2019).
- [54] Phung, M. D. & Ha, Q. P. Safety-enhanced uav path planning with spherical vector-based particle swarm optimization. *Applied Soft Computing* **107**, 107376 (2021).
- [55] Skrzypecki, S., Tarapata, Z. & Pierzchała, D. *Combined pso methods for uavs swarm modelling and simulation*, 11–25 (Springer,

2019).

- [56] Moreira, A. *et al.* A tutorial on synthetic aperture radar. *IEEE Geoscience and Remote Sensing Magazine* **1** (1), 6–43 (2013). <https://doi.org/10.1109/MGRS.2013.2248301>.
- [57] Li, C. J. & Ling, H. *Synthetic aperture radar imaging using a small consumer drone*, 685–686 (2015).
- [58] Rosen, P. A. *et al.* Synthetic aperture radar interferometry. *Proceedings of the IEEE* **88** (3), 333–382 (2000). <https://doi.org/10.1109/5.838084>.
- [59] Levanda, R. & Leshem, A. Synthetic aperture radio telescopes. *Signal Processing Magazine, IEEE* **27**, 14 – 29 (2010). <https://doi.org/10.1109/MSP.2009.934719>.
- [60] Dravins, D., Lagadec, T. & Nuñez, P. D. Optical aperture synthesis with electronically connected telescopes. *Nature communications* **6**, 6852 (2015). <https://doi.org/10.1038/ncomms7852>.
- [61] Ralston, T. S., Marks, D. L., Carney, P. S. & Boppart, S. A. Interferometric synthetic aperture microscopy (ISAM). *Nature Physics* 965–1004 (2007). <https://doi.org/10.1038/nphys514>.
- [62] Hayes, M. P. & Gough, P. T. Synthetic aperture sonar: a review of current status. *IEEE Journal of Oceanic Engineering* **34** (3), 207–224 (2009).
- [63] Hansen, R. E. in *Introduction to synthetic aperture sonar* (InTech Published, 2011). URL <http://www.intechopen.com/books/sonar-systems/introduction-to-synthetic-aperture-sonar>.
- [64] Jensen, J. A., Nikolov, S. I., Gammelmark, K. L. & Pedersen, M. H. Synthetic aperture ultrasound imaging. *Ultrasonics* **44**, e5 – e15 (2006). <https://doi.org/10.1016/j.ultras.2006.07.017>, in Proceedings of Ultrasonics International (UI'05) and World Congress on Ultrasonics (WCU).
- [65] Zhang, H. K. *et al.* Synthetic tracked aperture ultrasound imaging: design, simulation, and experimental evaluation. *Journal of medical imaging (Bellingham, Wash.)* **3** (27088108), 027001–027001 (2016). URL <https://www.ncbi.nlm.nih.gov/pmc/PMC4824841/>.
- [66] Barber, Z. W. & Dahl, J. R. Synthetic aperture lidar imaging demonstrations and information at very low return levels. *Applied optics* **53**, 5531–5537 (2014). <https://doi.org/10.1364/AO.53.005531>.
- [67] Turbide, S., Marchese, L., Terroux, M. & Bergeron, A. Synthetic aperture lidar as a future tool for earth observation. *Proc.SPIE* **10563**, 10563 – 10563 – 8 (2017). <https://doi.org/10.1117/12.2304256>.
- [68] Vaish, V., Wilburn, B., Joshi, N. & Levoy, M. *Using plane + parallax for calibrating dense camera arrays*, Vol. 1, I–I (2004).
- [69] Vaish, V., Levoy, M., Szeliski, R. & and, C. L. Z. *Reconstructing occluded surfaces using synthetic apertures: Stereo, focus and robust measures*, Vol. 2, 2331–2338 (2006).
- [70] Zhang, H., Jin, X. & Dai, Q. Hong, R., Cheng, W.-H., Yamasaki, T., Wang, M. & Ngo, C.-W. (eds) *Synthetic aperture based on plenoptic camera for seeing through occlusions*. (eds Hong, R., Cheng, W.-H., Yamasaki, T., Wang, M. & Ngo, C.-W.) *In Proceedings of Advances in Multimedia Information Processing – PCM 2018*, 158–167 (Springer International Publishing, Cham, 2018).
- [71] Yang, T. *et al.* Kinect based real-time synthetic aperture imaging through occlusion. *Multimedia Tools and Applications* **75** (12), 6925–6943 (2016). <https://doi.org/10.1007/s11042-015-2618-1>.
- [72] Joshi, N., Avidan, S., Matusik, W. & Kriegman, D. J. *Synthetic aperture tracking: Tracking through occlusions*, 1–8 (2007).
- [73] Pei, Z. *et al.* Occluded-object 3d reconstruction using camera array synthetic aperture imaging. *Sensors* **19** (3), 607 (2019).

- [74] Yang, T. *et al.* Fleet, D., Pajdla, T., Schiele, B. & Tuytelaars, T. (eds) *All-in-focus synthetic aperture imaging*. (eds Fleet, D., Pajdla, T., Schiele, B. & Tuytelaars, T.) *Computer Vision – ECCV 2014*, 1–15 (Springer International Publishing, Cham, 2014).
- [75] Pei, Z., Zhang, Y., Chen, X. & Yang, Y.-H. Synthetic aperture imaging using pixel labeling via energy minimization. *Pattern Recognition* **46** (1), 174–187 (2013) .
- [76] Kurmi, I., Schedl, D. C. & Bimber, O. Airborne optical sectioning. *Journal of Imaging* **4** (8), 102 (2018) .
- [77] Kurmi, I., Schedl, D. C. & Bimber, O. A statistical view on synthetic aperture imaging for occlusion removal. *IEEE Sensors Journal* **19** (20), 9374–9383 (2019) .
- [78] Kurmi, I., Schedl, D. C. & Bimber, O. Thermal airborne optical sectioning. *Remote Sensing* **11** (14), 1668 (2019) .
- [79] Kurmi, I., Schedl, D. C. & Bimber, O. Fast automatic visibility optimization for thermal synthetic aperture visualization. *IEEE Geoscience and Remote Sensing Letters* **18** (5), 836–840 (2020) .
- [80] Kurmi, I., Schedl, D. C. & Bimber, O. Combined person classification with airborne optical sectioning. *Scientific reports* **12** (1), 1–11 (2022) .
- [81] Kurmi, I., Schedl, D. C. & Bimber, O. Pose error reduction for focus enhancement in thermal synthetic aperture visualization. *IEEE Geoscience and Remote Sensing Letters* (2021) .
- [82] Bimber, O., Kurmi, I. & Schedl, D. C. Synthetic aperture imaging with drones. *IEEE computer graphics and applications* **39** (3), 8–15 (2019) .
- [83] Schedl, D. C., Kurmi, I. & Bimber, O. Airborne optical sectioning for nesting observation. *Nature Scientific Reports* **10** (1), 1–7 (2020) .
- [84] Amala Arokia Nathan, R. J., Kurmi, I. & Bimber, O. Inverse airborne optical sectioning. *Drones* **6** (9), 231 (2022) .
- [85] Eberhart, R. & Kennedy, J. *A new optimizer using particle swarm theory*, 39–43 (Ieee, 1995).
- [86] Kennedy, J. & Eberhart, R. C. *A discrete binary version of the particle swarm algorithm*, Vol. 5, 4104–4108 (IEEE, 1997).
- [87] Van Den Bergh, F. *et al.* *An analysis of particle swarm optimizers*. Ph.D. thesis, University of Pretoria (2007).
- [88] Van den Bergh, F. & Engelbrecht, A. P. A cooperative approach to particle swarm optimization. *IEEE transactions on evolutionary computation* **8** (3), 225–239 (2004) .
- [89] Coello Coello, C. & Leehuga, M. *Mgpsó: a proposal for multiple objective particle swarm optimization* (2002).
- [90] Gies, D. & Rahmat-Samii, Y. *Reconfigurable array design using parallel particle swarm optimization*, Vol. 1, 177–180 (IEEE, 2003).
- [91] Wang, D., Tan, D. & Liu, L. Particle swarm optimization algorithm: an overview. *Soft computing* **22** (2), 387–408 (2018) .
- [92] Freitas, D., Lopes, L. G. & Morgado-Dias, F. Particle swarm optimisation: a historical review up to the current developments. *Entropy* **22** (3), 362 (2020) .
- [93] Rutherford, E. Lxxix. the scattering of  $\alpha$  and  $\beta$  particles by matter and the structure of the atom. *The London, Edinburgh, and Dublin Philosophical Magazine and Journal of Science* **21** (125), 669–688 (1911) .
- [94] Reed, I. S. & Yu, X. Adaptive multiple-band cfar detection of an optical pattern with unknown spectral distribution. *IEEE transactions on acoustics, speech, and signal processing* **38** (10), 1760–1770 (1990) .
- [95] Seits, F., Kurmi, I. & Bimber, O. Evaluation of color anomaly detection in multispectral images for synthetic aperture sensing. *Eng*



3 (4), 541–553 (2022) .

- [96] Suzuki, S. *et al.* Topological structural analysis of digitized binary images by border following. *Computer vision, graphics, and image processing* **30** (1), 32–46 (1985) .
- [97] Stephenson, K. *Introduction to circle packing: The theory of discrete analytic functions* (Cambridge University Press, 2005).
- [98] Pirl, U. The minimum distance of  $n$  points located in the unit disk. *Math News* **40** (1-3), 111–124 (1969) .
- [99] Greening, M., Graham, R. & Ratz, J. Sets of points with given minimum separation. *AMERICAN MATHEMATICAL MONTHLY* **75** (2), 192 (1968) .
- [100] Melissen, H. Densest packings of eleven congruent circles in a circle. *Geometriae Dedicata* **50** (1), 15–25 (1994) .
- [101] Fodor, F. The densest packing of 19 congruent circles in a circle. *Geometriae Dedicata* **74** (2), 139–145 (1999) .
- [102] Fodor, F. The densest packing of 12 congruent circles in a circle. *Beiträge Algebra Geom* **41**, 401–409 (2000) .
- [103] Fodor, F. The densest packing of 13 congruent circles in a circle. *Beiträge zur Algebra und Geometrie* **44** (2), 431–440 (2003) .
- [104] Graham, R. L., Lubachevsky, B. D., Nurmela, K. J. & Östergård, P. R. Dense packings of congruent circles in a circle. *Discrete Mathematics* **181** (1-3), 139–154 (1998) .

**Data and Code Availability.** All experimental data presented in this article is available at: <https://doi.org/10.5281/zenodo.7472380>

The simulation code used to compute all results presented in this article is available at: <https://github.com/JKU-ICG/AOS> (AOS for Drone Swarms).

**Acknowledgments.** This research was funded by the Austrian Science Fund (FWF) under grant number P32185-NBL and by the State of Upper Austria and the Austrian Federal Ministry of Education, Science and Research via the LIT–Linz Institute of Technology under grant number LIT-2019-8-SEE114.

**Author Contributions.** O.B. developed the concept, conceived and designed the algorithm and experiments. R.J.A.A.N. and I.K. implemented the algorithm and performed the experiments. R.J.A.A.N., I.K. and O.B. analysed the data, contributed materials, and wrote the paper.

**Competing Interests.** The authors declare no competing interests.

# Supplementary Material

## S1 Simulated vs. Real Integrals

Figure S1 illustrates the difference between integral images that are simulated for our procedural forest and integral images that are captured with a physical drone over real mixed forest. Both show an upright standing person (blue cloth, black hair). Note that sensor errors, such as GPS imprecision or camera noise, are not simulated and that the cloth color of the avatar in the simulation was only roughly matched with the cloth color of the real person. In contrast to the the simulations, real integrals suffer from artifacts and blur that are due to misregistrations caused by GPS errors and camera noise. This example, however, indicates that simulated integrals approximate real integrals well, and that our simulations are not too far from real-world conditions.

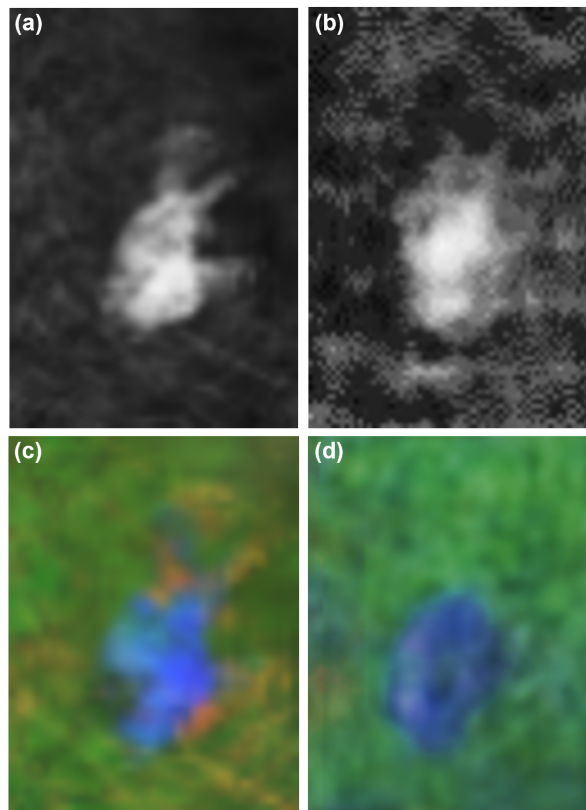


**Fig. S1** Simulated integral images for our procedural forest (a: thermal, c: RGB) versus integral images captured with a physical camera drone above real mixed forest (b: thermal, d: RGB). The close-ups are scaled to the same dimensions on the forest ground.

## S2 Different vs. Same Altitude

Figure S2 visualizes the difference of simulated integral images computed for drones with varying altitudes (as explained in **Collision Avoidance**) versus integral images that are computed for drones with the same altitude. Note that sensor errors, such as GPS imprecision or camera noise, are not simulated. They would add additional blur and noise in both cases, which would make the difference between the two cases even less. Note also that minor difference are also due to perspective changes caused by the different altitudes, while spatial sampling remains mainly unaffected.

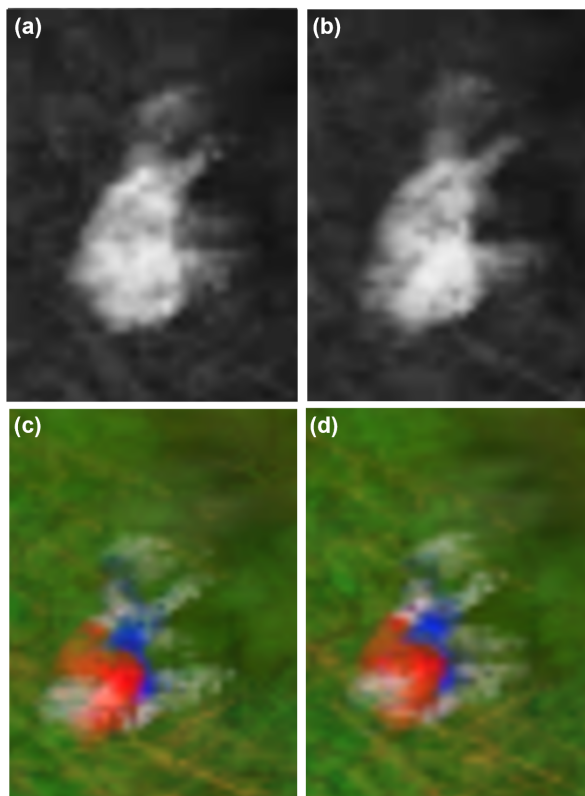


**Fig. S2** Simulated integral images computed for drones with various altitudes (a: thermal, c: RGB, altitude range: 35-44  $m$  at 1  $m$  steps) versus simulated integral images computed for drones with the same (average of 35-44  $m$ ) altitude (b: thermal, d: RGB, altitude: 40  $m$ ). Note that the lateral positions of the ( $n = 10$ ) drones are identical in both cases.

### S3 Another Motion Example

In Fig. S3, another motion example is illustrated. Here, the target moves on a circular path, without stopping. Although the swarm loses it due to too dense occlusions at the bottom-left and bottom-right parts of the path, it is able to re-detect and track it till the end. The average deviation between the target's ground truth position, motion speed, motion direction and the corresponding estimations of our PSO was  $0.53\text{ m}$ ,  $0.088\text{ m/s}$ , and  $10.35^\circ$ , respectively.

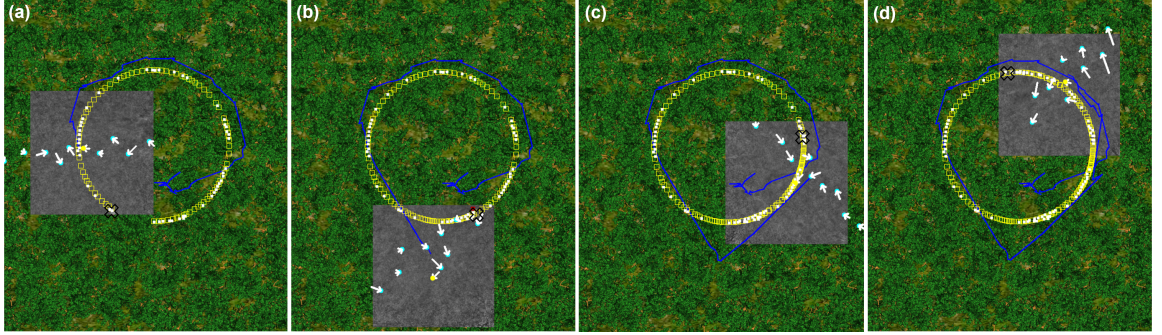


**Fig. S3** Tracking a person moving on a circular path at constant speed ( $4\text{ m/s}$ ): The target is lost after 29.71 seconds (a), re-detected after 32.32 seconds (b), lost again after 34.88 seconds, re-detected after 39.628 seconds (c), and tracked for the remaining 8.17 seconds (d). Note that the yellow boxes highlight the target's ground truth positions, the white stars indicate the target's estimated positions, the white arrows show the movement of the drones between time steps  $t - 1$  and  $t$ , the blue lines represent the total sampling paths of the swarm's center of gravity, the yellow dots indicate the the best sampling position at time  $t$ , the grey area illustrates the integrated ground coverage at time  $t$ , and the black crosses indicate the target's position at the presented simulation times. Simulation parameters (see **Methods** for details): drones' ground speed =  $10\text{ m/s}$ ,  $\Delta_h = 1\text{ m}$ , forest density =  $300\text{ trees/ha}$ ,  $n = 10$ ,  $T = 20.4\%$ ,  $h_1 = 35\text{ m}$ ,  $c_1 = 1\text{ m}$ ,  $c_2 = 2\text{ m}$ ,  $c_3 = 1.643\text{ m}$ ,  $s = c_4 = 4.2\text{ m}$ ,  $c_5 = 0.3$ . See Supplementary Video 6.

### S4 Visibility Probability for Parallel-Sequential Sampling in Presence of Motion

Here we present the derivation of the visibility in an integral image  $X$  (as defined in [77]) of a hypothetical occlusion-free reference target signal  $S$  of size  $S_l$  moving at speed  $S_v$ .

The integral image  $X$  is the average of total  $N$  single images, where  $N = N_p \cdot N_s$  ( $N_s$  sequential instances, being  $\Delta t$  apart from each other, of  $N_p$  images recorded in parallel at any instance  $t$ ). Compared to our previous model, where the target signal  $S$  was static, a moving target signal  $S$  can now be present at any location in only  $N_o$  instances (where  $N_o = \frac{S_l}{(S_v \cdot \Delta t)}$ ) and  $N_v$  ( $N_v = N_p \cdot \text{Min}(N_o, N_s)$ ) images.

Out of  $N$  image recordings, each single pixel pertaining to the target signal can be either occlusion free or occluded in only  $N_v$  images. We model this by the random variables:  $S$  (occlusion free),  $O$  (occluded),  $Z$  (determines if occluded or not), and  $D$  (occlusion probability). In  $N_v$  single image recordings, a pixel is  $D$  likely occluded ( $Z_i = 1$ ). In this case the pixel's content is  $O_i$ . Otherwise it is  $(1 - D)$  likely occlusion free ( $Z_i = 0$ ). In this case it contains  $S$ :

$$X = \frac{1}{N} \left( \sum_{i=1}^{N_v} (Z_i O_i + (1 - Z_i) S) + \sum_{i=N_v+1}^N O_i \right). \quad (\text{S1})$$

All random variables are independent and identically distributed with  $Z_i$ , following a Bernoulli distribution with success parameter  $D$  (i.e.,  $E[Z_i] = E[Z_i^2] = D$ ; furthermore, note that  $E[Z_i(1 - Z_i)] = 0$  is true). The random variable  $S$  follows a distribution with mean  $E[S] = \mu_s$  and  $E[S^2] = (\mu_s^2 + \sigma_s^2)$  and analogously  $O_i$  follows a distribution with mean  $E[O_i] = \mu_o$  and  $E[O_i^2] = (\mu_o^2 + \sigma_o^2)$ .

From [77], visibility is given by

$$V = 1 - \text{MSE}, \quad (\text{S2})$$

where

$$\text{MSE} = \text{E}[(X - S)^2] = \text{E}[X^2] - 2\text{E}[XS] + \text{E}[S^2]. \quad (\text{S3})$$

Thus the first term of Eqn. S3 expands to

$$\text{E}[X^2] = \text{E} \left[ \left( \frac{1}{N} \left( \sum_{i=1}^{N_v} Z_i O_i + (1 - Z_i) S + \sum_{i=N_v+1}^N O_i \right) \right)^2 \right], \quad (\text{S4})$$

$$\text{E}[X^2] = \frac{1}{N^2} \text{E} \left[ \left( \sum_{i=1}^{N_v} Z_i O_i + (1 - Z_i) S + \sum_{i=N_v+1}^N O_i \right) \left( \sum_{k=1}^{N_v} Z_k O_k + (1 - Z_k) S + \sum_{k=N_v+1}^N O_k \right) \right]. \quad (\text{S5})$$

By distributive law,

$$\begin{aligned} \text{E}[X^2] = & \frac{1}{N^2} \text{E} \left[ \left( \sum_{i=1}^{N_v} Z_i O_i + (1 - Z_i) S \right) \left( \sum_{k=1}^{N_v} Z_k O_k + (1 - Z_k) S \right) \right. \\ & + \left( \sum_{i=1}^{N_v} Z_i O_i + (1 - Z_i) S \right) \left( \sum_{k=N_v+1}^N O_k \right) + \left( \sum_{i=N_v+1}^N O_i \right) \left( \sum_{k=1}^{N_v} Z_k O_k + (1 - Z_k) S \right) \\ & \left. + \left( \sum_{i=N_v+1}^N O_i \right) \left( \sum_{k=N_v+1}^N O_k \right) \right]. \quad (\text{S6}) \end{aligned}$$

Again applying the distributive law, we get terms where  $i = k$  and terms where  $i \neq k$ :

$$\begin{aligned} \text{E}[X^2] = & \frac{1}{N^2} \text{E} \left[ \sum_{i=1}^{N_v} (Z_i O_i + (1 - Z_i) S)^2 + \sum_{i=1}^{N_v} \sum_{k \neq i}^{N_v} (Z_i O_i + (1 - Z_i) S) (Z_k O_k + (1 - Z_k) S) \right. \\ & + \sum_{i=1}^{N_v} \sum_{k=N_v+1}^N Z_i O_i O_k + \sum_{i=1}^{N_v} \sum_{k=N_v+1}^N (1 - Z_i) S O_k + \sum_{i=N_v+1}^N \sum_{k=1}^{N_v} Z_k O_k O_i \\ & \left. + \sum_{i=N_v+1}^N \sum_{k=1}^{N_v} (1 - Z_k) S O_i + \sum_{i=N_v+1}^N O_i^2 + \sum_{i=N_v+1}^N \sum_{k \neq i}^N O_i O_k \right], \quad (\text{S7}) \end{aligned}$$

which further simplifies to

$$\begin{aligned} \text{E}[X^2] = & \frac{1}{N^2} \left[ N_v (D (\mu_o^2 + \sigma_o^2) + (1 - D) (\mu_s^2 + \sigma_s^2)) \right. \\ & + N_v (N_v - 1) (D^2 \mu_o^2 + 2D (1 - D) \mu_s \mu_o + (1 - D)^2 (\mu_s^2 + \sigma_s^2)) \\ & + 2N_v (N - N_v) (D \mu_o^2 + (1 - D) \mu_s \mu_o) \\ & \left. + (N - N_v) (\mu_o^2 + \sigma_o^2) + (N - N_v)(N - N_v - 1) \mu_o^2 \right]. \quad (\text{S8}) \end{aligned}$$



The second term of Eqn. S3 expands to

$$E[XS] = \frac{1}{N} E [Z_i O_i S + (1 - Z_i) S^2 + O_i S], \quad (\text{S9})$$

$$E[XS] = \frac{1}{N} [N_v (D\mu_o\mu_s + (1 - D) (\mu_s^2 + \sigma_s^2)) + (N - N_v) \mu_o\mu_s]. \quad (\text{S10})$$

Using the expanded terms in S8 & S10 in S3,

$$\begin{aligned} \text{MSE} = & \frac{1}{N^2} \left[ \mu_o^2 (N_v D (1 + (N_v - 1) D + 2 (N - N_v)) + (N - N_v)^2) \right. \\ & + \sigma_o^2 (N_v D + N - N_v) \\ & + (\mu_s^2 + \sigma_s^2) (N_v (1 - D) (1 + (N_v - 1) (1 - D))) \\ & \left. + \mu_s \mu_o (2N_v (N_v - 1) D (1 - D) + 2N_v (N - N_v) (1 - D)) \right] \\ & - \frac{2}{N} \left[ N_v (D\mu_o\mu_s + (1 - D) (\mu_s^2 + \sigma_s^2)) + (N - N_v) \mu_o\mu_s \right] + (\mu_s^2 + \sigma_s^2), \end{aligned} \quad (\text{S11})$$

$$\begin{aligned} \text{MSE} = & \frac{1}{N^2} \left[ \mu_o^2 (N_v D (1 - D) + (N - N_v + N_v D)^2) \right. \\ & + \sigma_o^2 (N_v D + N - N_v) \\ & + (\mu_s^2 + \sigma_s^2) (N_v (1 - D) (D + N_v (1 - D))) \\ & \left. + 2\mu_s \mu_o (N_v (1 - D) ((N_v - 1) D + (N - N_v))) \right] \\ & - \frac{2}{N} \left[ N_v (D\mu_o\mu_s + (1 - D) (\mu_s^2 + \sigma_s^2)) + (N - N_v) \mu_o\mu_s \right] + (\mu_s^2 + \sigma_s^2), \end{aligned} \quad (\text{S12})$$

$$\begin{aligned} \text{MSE} = & \mu_o^2 \left( \frac{N_v D (1 - D)}{N^2} + \left( 1 - \frac{N_v (1 - D)}{N} \right)^2 \right) \\ & + (\mu_s^2 + \sigma_s^2) \left( \frac{N_v D (1 - D)}{N^2} + \left( 1 - \frac{N_v (1 - D)}{N} \right)^2 \right) \\ & + 2\mu_o\mu_s \left( \frac{N_v (1 - D)}{N^2} ((N_v - 1) D + (N - N_v)) - \frac{N_v D}{N} - \frac{(N - N_v)}{N} \right) \\ & + \sigma_o^2 \left( \frac{(N_v D + N - N_v)}{N^2} \right), \end{aligned} \quad (\text{S13})$$

$$\begin{aligned} \text{MSE} = & \left[ \left( 1 - \frac{N_v (1 - D)}{N} \right)^2 + \frac{N_v D (1 - D)}{N^2} \right] \left( \sigma_s^2 + (\mu_o - \mu_s)^2 \right) \\ & + \left( \frac{(N_v D + N - N_v)}{N^2} \right) \sigma_o^2. \end{aligned} \quad (\text{S14})$$

Substituting Eqn. S14 in Eqn. S2,

$$\begin{aligned} V = 1 - & \left[ \left( 1 - \frac{N_v (1 - D)}{N} \right)^2 + \frac{N_v D (1 - D)}{N^2} \right] \left( \sigma_s^2 + (\mu_o - \mu_s)^2 \right) \\ & - \left( \frac{(N_v D + N - N_v)}{N^2} \right) \sigma_o^2. \end{aligned} \quad (\text{S15})$$